JOURNAL OF MATERIALS SCIENCE 28 (1993) 2196–2206

Toughness and fatigue of encapsulation-processed silicon carbide–polymer matrix particulate composites

CHI SHEU*, R. H. DAUSKARDT, L. DE JONGHE
Materials Science Division, Lawrence Berkeley Laboratory, and Department of Materials Science and Mineral Engineering, University of California, Berkeley, CA 94720, USA

A new process for composite fabrication was developed which improves distribution of the particulate reinforcing phase by polymer encapsulation of the particulate prior to consolidation. The effect of such processing on the fatigue-crack propagation and fracture toughness behaviour of particulate thermoplastic composites was investigated. Composites of several particulate size ranges were fabricated into disc-shaped, compact tension specimens and tested under cyclic and monotonic loading conditions. For comparison, a composite was also fabricated using a standard casting technique. The observed fatigue-crack growth rates spanned three orders of magnitude (10^{-11} to 10^{-9} m per cycle) over an applied stress intensity range, ΔK, of 0.3 to 1.1 MPa $m^{1/2}$. The measured fracture toughness values ranged from 0.69 to 2.95 MPa $m^{1/2}$. Comparison of the two processing techniques indicated that encapsulation processing increased the fracture toughness of the composite by approximately 33%; however, the fatigue-crack growth behaviour was unaffected. In addition, a trend of increasing crack growth resistance (toughness) with increasing reinforcement particle size was observed. These results are discussed in the light of crack shielding and bridging models for composite toughening.

1. Introduction

The incorporation of second-phase reinforcements into polymer matrices has widened the applicability of polymers by enhancing key physical and structural properties. Specific properties may be improved by the proper combination of matrix resin and reinforcement phase. In this fashion, custom-tailored composites can be produced to satisfy a wide range of applications. Improved mechanical properties, abrasion and corrosion resistance, and reduced structural weight and cost are some of the advantages when composites replace conventional metallic materials.

Particulate reinforcements have traditionally been utilized to enhance secondary physical properties of composites, whereas fibre reinforcements were used primarily to enhance mechanical strength. Due to the advantages of their isotropic mechanical properties, particulate composites have more recently been exploited in structural applications. As a result, several studies have been undertaken to address the effect of reinforcements on the crack propagation behaviour of this class of composites [1–3].

Particulate composites are generally fabricated by mechanically incorporating reinforcement during polymerization through shear mixing, which requires good reinforcement wetting by the polymer. In particular, wetting is highly dependent on the surface area to be wet, as well as on the viscosity of the wetting liquid. As surface area is increased, either by an increase in the volume fraction of filler or by a decrease in filler particle size, uniform polymer wetting becomes more difficult. To improve wetting, the viscosity of the system can be reduced. However, since suspension stability decreases with decreasing viscosity, excessive settling may occur, leading to non-uniform particulate distributions. Consequently, the volume fraction and size of reinforcement that can be uniformly dispersed by shear mixing is limited. The maximum attainable composite properties are therefore constrained by the wetting/uniformity trade-off established by processing limitations. Furthermore, the casting processes typically employed in particulate composite fabrication induce residual stresses as a result of matrix shrinkage during polymerization. Since studies have shown that the mechanical properties of particulate composites are significantly influenced by the reinforcement size [1], volume fraction [4–6], distribution [7, 8] and residual stress levels [9], an alternative to shear mix processing/casting may result in significant mechanical property benefits.

The processing flexibility necessary to provide an alternative to shear mixing is afforded by thermoplastic resins. Thermoplastics have two major advantages as matrix resins. Firstly, the mechanical strength of

* Present address: Northrop Corporation, Hawthorne, CA 90250-3277, USA.

0022–2461

thermoplastics is derived from the physical entanglement of long molecular chains. The rotational freedom of these linear chains results in resins capable of absorbing substantial energy without damage. This is in contrast to thermosets which depend upon chemical cross-linking to achieve mechanical strength, with high cross-link densities required for high strength. Such high cross-link densities, however, often result in brittleness. Secondly, thermoplastics offer the advantage of reprocessability. Since the physical entanglement of molecular chains is a reversible process, thermoplastics can be reprocessed by heating above their flow temperature and reconsolidated. For thermosetting systems, however, the molecular configuration is frozen once cross-linking has occurred and the resin can no longer be manipulated. The processing flexibility exhibited by thermoplastics therefore allows the consolidation of complex composite parts with relative ease.

The reprocessability of thermoplastics can also be exploited to produce composites of high filler content and/or fine reinforcement particles with uniform dispersion through encapsulation processing. By selectively encapsulating the individual reinforcement particles with a thermoplastic polymer prior to consolidation, a uniform particulate distribution is assured. In addition, since the polymer is cured prior to consolidation, shrinkage stresses associated with the cure are eliminated from the composite. Finally, a wide range of particulate size ranges may be processed due to the elimination of suspension stability concerns. The purpose of this study, therefore, is to investigate the impact of this novel processing approach on the crack propagation behaviour of particulate composites.

2. Experimental procedure

2.1. Encapsulation processing

For the task of reinforcement particle encapsulation, a precipitation polymerization process was employed. This process has been successfully applied to the encapsulation of finely divided pigment particles in the paint industry [10]. In the present study, polymethyl methacrylate (PMMA) and β-silicon carbide were selected for the matrix resin and reinforcement phase, respectively. PMMA is a typical aliphatic amorphous thermoplastic polymer that is suitable for precipitation processing. Silicon carbide is frequently used as a brittle second-phase reinforcement in particulate composites. Particulate sizes of 1, 16, and 100 μm were encapsulated, with a constant filler volume fraction of 30%. This volume fraction has been shown to be optimum for enhancing the mechanical properties of the composite while minimizing fracture toughness degradation [4].

β-silicon carbide powder was prepared by mechanical grinding followed by sieving to remove large agglomerates and any coarse fractions. A measured quantity was ultrasonically dispersed in a distillation flask containing hexane to break up any remaining agglomerates. The solution was heated to boiling under a distillation column and agitated to maintain suspension. The monomer solution was separately prepared by dissolving a quantity of methyl methacrylate into hexane. The ratio of silicon carbide to methyl methacrylate selected to maintain the desired filler volume fraction was determined by iteration. Finally, a solution containing 1 wt % benzoyl peroxide in toluene was prepared to provide polymerization initiation.

The prepared solutions were introduced dropwise into the suspension over a period of 2 h with agitation and allowed to react for an additional 2 h. The reaction product was transferred to a large container and the excess solvent decanted. The slurry remaining following solvent removal was allowed to stand until a firm consistency was reached. A powder cake was formed by vacuum-drying the slurry for 2 h to remove the remaining solvent. As an alternative, the reaction product can be spray-dried directly to produce the final powder product. The volume fraction of silicon carbide following encapsulation was determined through polymer burnout measurements.

2.2. Composite fabrication

Following particle encapsulation, composites of different particle size ranges were formed by compression-moulding the powder in a 1 in. (25 mm) diameter die press. A pressure of 27 MPa was applied at 150 °C for 20 min. To facilitate comparison, a baseline composite system containing 30 vol % of 100 μm β-silicon carbide particles was also prepared using a conventional shear mixing/casting technique.

To fabricate the cast composite, silicon carbide particles were first prepared by mechanical grinding and sieving. A measured quantity of methyl methacrylate was introduced into a small container. 1 wt % benzoyl peroxide (initiator) and 0.03 vol % N,N-dimethyl p-toluidine (accelerator) were added. Because of the volatile nature of the reactants, the container was sealed to prevent reactant evaporation during polymerization. When the viscosity of the polymerizing system increased sufficiently to minimize particulate settling, the silicon carbide was incorporated and mechanically agitated for maximum dispersion. The mixture was poured into 1 in. (25 mm) diameter mould-released rings placed on a glass plate and allowed to set. The moulds were cured at 110 °C for 1 h to complete polymerization.

The blank composite discs were machined to form disc-shaped compact tension DC(T) specimens with dimensions scaled to ASTM Standard E 647 requirements [11]. Typical dimensions include a specimen width (W) of 17.5 mm, thickness (B) of approximately 2 mm, and an initial notch length of 11.5 mm (Fig. 1a). The radially edge-cracked disc configuration has been shown to be very effective for the testing of PMMA when compared to other standard geometries [12]. To facilitate post-fracture crack profile evaluation, the specimen faces were polished. The specimens were tested under both cyclic fatigue and static loading conditions.

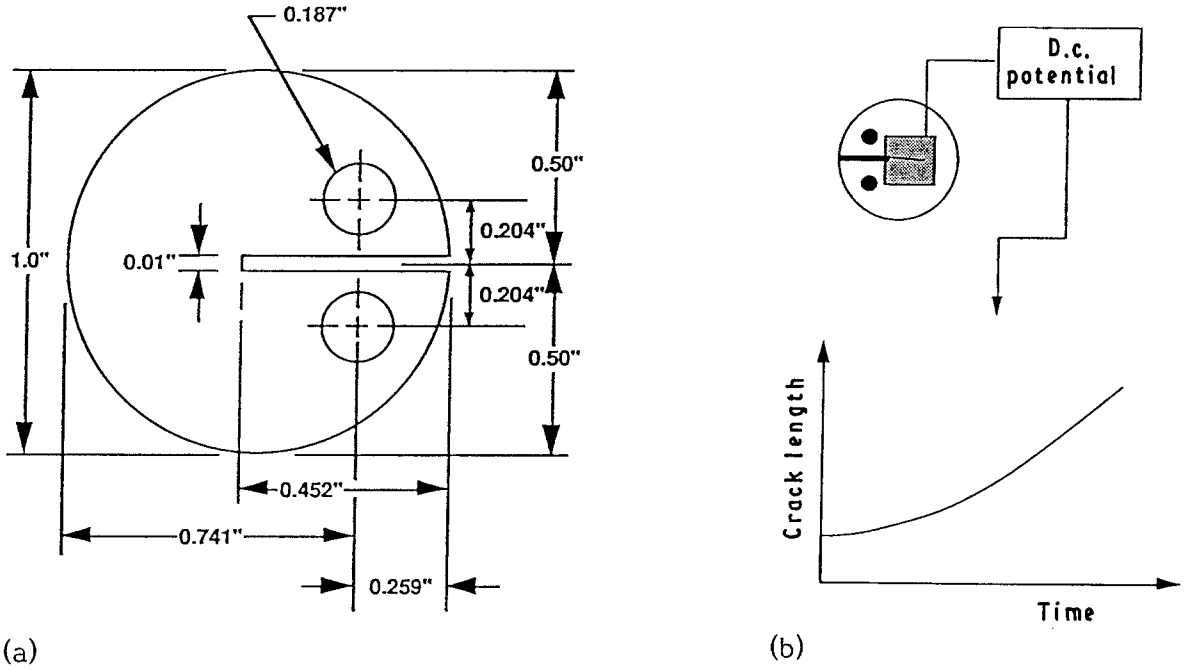

Figure 1 Schematic illustration of experimental arrangement showing (a) the disc-shaped compact tension DC(T) geometry, and (b) the d.c. electrical potential drop technique used to monitor crack length. 1″ = 25.4 mm.

2.3. Fatigue-crack growth testing

Cyclic fatigue-crack propagation rates (da/dN) were determined using methods developed by Dauskardt and Ritchie [13] for testing of brittle solids*, in general accordance with the current ASTM Standard E647-86A for measurements of constant-load amplitude fatigue crack growth rates [11]. Crack growth rates were determined as a function of the applied stress-intensity range, ΔK, obtained from linear-elastic fracture mechanics. For the DC(T) test specimens, stress intensity values were computed from handbook solutions [11] in terms of the applied load P and crack length a as

$$K = \frac{P}{BW^{1/2}} f(a/W)$$

where for $0.3 < a/W < 1$

$$f(a/W) = \frac{[2 + (a/W)][0.76 + 4.8(a/W) - 11.58(a/W)^2 + 11.43(a/W)^3 - 4.08(a/W)^4]}{[1 - (a/W)]^{3/2}} \quad (1)$$

Under cyclic loading the stress-intensity range ΔK is given by

$$\Delta K = K_{max} - K_{min} \quad (2)$$

where K_{max} and K_{min} are the maximum and minimum values of the applied loading cycle, respectively.

Fatigue-crack propagation tests were performed in controlled room-temperature (22 °C) environments at a sinusoidal frequency of 50 Hz and a load ratio R (ratio of K_{min} to K_{max}) of 0.1 using an electro-servohydraulic mechanical testing system with associated high-speed data acquisition and computer control. Tests were carried out under either closed-loop displacement or stress-intensity control. The threshold stress intensity range below which crack growth is presumed dormant, ΔK_{TH}, was defined at growth rates below 10^{-11} m per cycle, following ASTM E647 standard procedure. Under computer control, thresholds were approached by varying the applied loads so that the instantaneous values of crack length a and stress intensity range ΔK varied according to

$$\Delta K = \Delta K_0 \exp[C^*(a - a_0)] \quad (3)$$

where a_0 and ΔK_0 are the initial values of a and ΔK, and C^* is the normalized K-gradient $(1/K)(dK/da)$, set to -0.09 per mm of crack extension.

Crack initiation was achieved by machining a wedge-shaped starter notch of approximately 2 mm in length, from which a fatigue crack was carefully grown under displacement control.

Crack length was continuously monitored *in situ* by means of d.c. electrical potential techniques [14]. Thin (20 μm) Ni–Cr metal foils were bonded to the specimen surface and changes in electrical potential with crack extension (at constant current) monitored. These measurements were relayed to the computer for control and data processing (Fig. 1b). Crack-growth rates, da/dN, were determined automatically by numerical differentiation of measurements of crack length a as a function of the number of cycles, N. The data are presented on a standard log–log graph of da/dN as a function of ΔK.

* Note that while the PMMA matrix is not considered a brittle material, the incorporation of a brittle SiC second phase does result in markedly lower ductility and fracture toughness values, thereby requiring the advanced mechanical testing techniques developed for brittle solids.

2.4. Fracture toughness testing

Following completion of the sub-critical crack-growth test, the composite fracture toughness was determined. The specimens containing a fatigue pre-crack were loaded under displacement control and the resistance-curve (R-curve) behaviour analysed using techniques which generally conform to ASTM Standard E399-87 for the plane-strain fracture toughness of metallic materials [15]. The data are presented as a graph of stress intensity K_I as a function of crack extension Δa. Values of the fracture toughness were defined at crack initiation K_i and at the steady-state plateau, K_c, on this curve.

3. Results

3.1. Encapsulation processing

Scanning electron microscopy examination after the precipitation polymerization process revealed that the SiC particles were fully encapsulated, with only minor residual agglomeration between encapsulated particles. A representative SEM micrograph showing fully encapsulated particles is presented in Fig. 2. For comparison, homogeneously precipitated particles of PMMA using the same process parameters, but omitting the reinforcement particles, are shown in Fig. 3. The interface formed between the polymer and SiC particle substrate was analysed using transmission electron microscopy. The encapsulation process produced a well-adhered continuous interface, as apparent in Fig. 4. As expected, no crystalline features were observed in the polymer coating.

3.2. Cyclic fatigue crack-growth

The fatigue crack-growth rates, da/dN, for encapsulation-processed and conventionally cast composites are plotted as a function of the applied stress intensity range, ΔK, for $R = 0.1$ in Fig. 5. Data taken from the literature for an unreinforced PMMA are included for comparison* [16]. Crack growth rates span three orders of magnitude from 10^{-11} to 10^{-9} m per cycle, over a range of ΔK from ~ 0.3 to 1.1 MPa $m^{1/2}$. Similar to behaviour in metals [17] and many ceramics (see e.g. [18]), crack growth data appear to follow a conventional Paris power-law relationship over the range of growth rates measured, with

$$da/dN = C(\Delta K)^m \quad (4)$$

where C and m are constants typically dependent on the material and testing conditions. Values of C and m for the composites tested are included in Table I.

Each composite displayed an apparent fatigue threshold, ΔK_{TH}, below which no crack growth is observed. The fatigue threshold was determined by decreasing ΔK until crack growth was essentially arrested. Measured values of ΔK_{TH} ranged from 0.36 to 0.71 MPa $m^{1/2}$.

A trend of increasing resistance to cyclic fatigue crack growth with increasing particle size is clearly exhibited. At low growth rates, the 16 μm (EP16) and the 100 μm (EP100) particle size composites exhibited

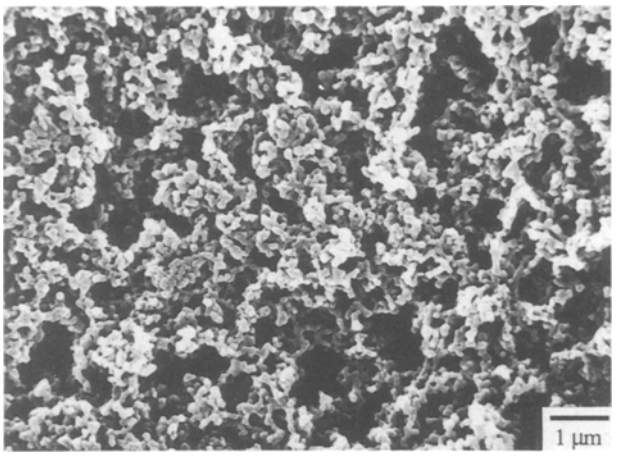

Figure 3 SEM micrograph showing homogeneously precipitated PMMA.

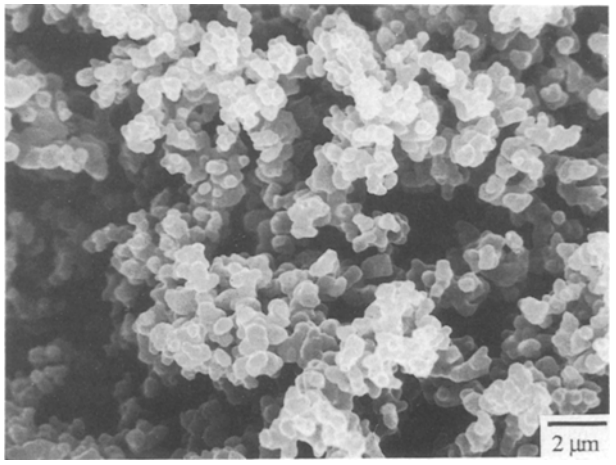

Figure 2 SEM micrograph showing PMMA-encapsulated SiC particles.

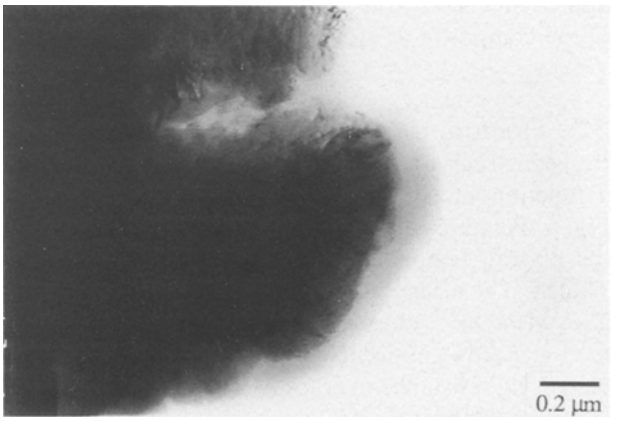

Figure 4 TEM micrograph showing the SiC-particle–PMMA interface.

* Note that fatigue crack growth behaviour in polymeric materials is sensitive not only to the molecular weight and arrangement (e.g. extent of cross-linking and entanglement), but also to fatigue variables such as cyclic frequency, load ratio, etc. [16]. Comparisons with data reported in the literature should therefore be treated with appropriate caution.

TABLE I Measured values of fracture toughness at initiation K_i and steady-state K_c, and fatigue threshold ΔK_{TH} and crack-growth parameters m and c, for the composites tested

Composite	Fracture toughness		Fatigue		
	K_i (MPa $m^{1/2}$)	K_c (MPa $m^{1/2}$)	ΔK_{TH} (MPa $m^{1/2}$)	m	c (m/cycle (MPa $m^{1/2}$) $^{-m}$)
EP1	0.70	0.71	0.36	6	5.40×10^{-7}
EP16	1.29	1.50	0.6	13	1.13×10^{-7}
EP100	2.37	2.95[a]	0.7	15	1.89×10^{-8}
CC100	1.64	2.22	0.7	18	5.89×10^{-8}

[a] Extrapolated value.

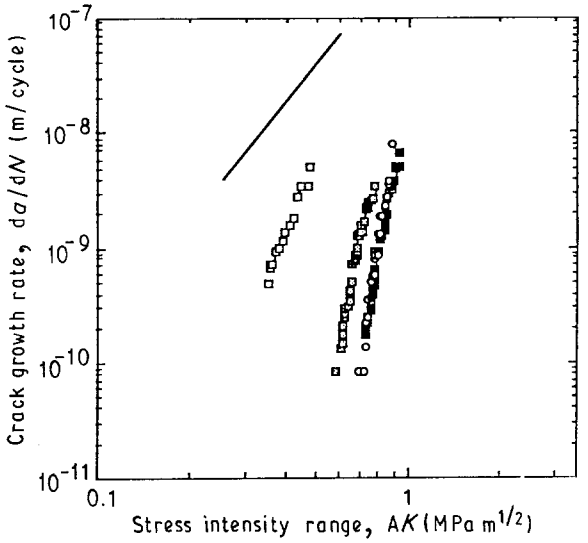

Figure 5 Fatigue crack growth behaviour, in terms of growth rates per cycle, da/dN, as a function of the applied stress-intensity range, ΔK, for encapsulation-processed (EP) and cast/mixed (CC) particulate-reinforced PMMA-matrix composites with 30 vol % SiC: (□) EP1, (▨) EP16, (■) EP100, (○) CC100. (——) data for unreinforced PMMA taken from the literature [16], included for comparison.

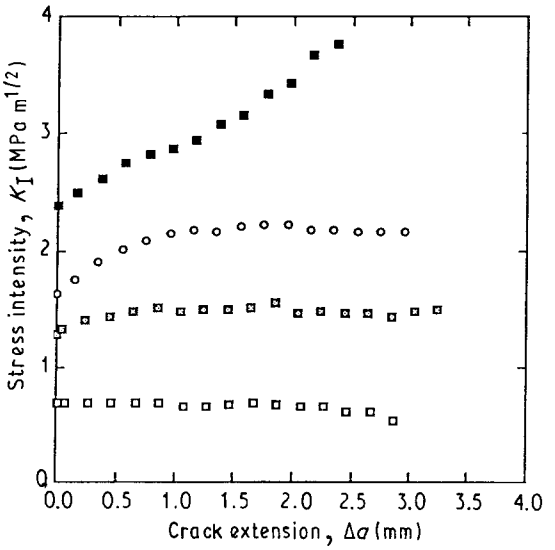

Figure 6 Fracture-toughness behaviour in the form of resistance curves (R-curves) for the encapsulation-processed (EP) and the cast/mixed (CC) particulate-reinforced PMMA-matrix composites with 30 vol % SiC: (□) EP1, (▨) EP16, (■) EP100, (○) CC100.

fatigue thresholds some 67 and 95% higher, respectively, than the 1 μm (EP1) material. Similar growth rates, however, were observed for the shear mixed/cast composite (CC100) and the encapsulation-processed material (EP100), indicating that the two processing approaches have little influence on the susceptibility of the composite to cyclic fatigue.

3.3. Fracture toughness

Resistance curves, showing fracture toughness data as a function of crack extension Δa are presented in Fig. 6. Toughness values at crack initiation K_i and at the plateau region of the R-curve, K_c, are listed in Table I. The measured toughness ranged from 0.69 to 2.37 MPa $m^{1/2}$ at K_i and from 0.71 to 2.95 MPa $m^{1/2}$ at K_c. No noticeable R-curve behaviour, that is, increasing resistance to crack extension, was observed for the 1 μm particle size composite, which displayed a relatively constant fracture toughness with crack length.

As the fracture toughness testing was conducted on samples with fatigue pre-cracks, the measured values may differ from those measured from notched samples. While the plateau values, K_c, are likely to be more conservative due to the "atomically sharp" nature of the crack tip, the initiation values, K_i, may be higher, reflecting the highest K_{max} experienced during the prior fatigue test. For design considerations, K_c obtained from fatigue pre-cracked samples represents a lower bound of the maximum toughness value for the composite.

No steady-state plateau was observed for composite EP100, although an onset can be seen. Consequently, the K_c value for composite EP100 was determined by extrapolation from the position of first inflection of the R-curve. The sustained increase in crack growth resistance with increasing crack extension is likely to be due to a large-scale bridging effect, and not from any intrinsic toughening mechanisms. Such behaviour may occur when the absolute size of the bridging zone approaches in-plane specimen dimensions [19]. However, this has not been experimentally verified in the present study.

Consistent with cyclic fatigue results, fracture toughness values were observed to increase with increasing particle size, resulting from the greater effectiveness of large reinforcement particles. Contrary to the fatigue results, however, a significant improvement in fracture toughness was observed for the encapsulation-processed composite compared to the shear

mixed/cast material. These data indicate that the processing approach plays an important role in the crack propagation resistance of particulate composites.

3.4. Fracture surface morphology

Representative SEM micrographs indicating typical fracture surface morphology for the encapsulation-processed composites tested are shown in Fig. 7a–c for fatigue loading and Fig. 7d–f for the R-curve fracture tests. Similar micrographs for the mixed/cast composite are shown in Fig. 8. An increasingly rough fracture morphology was apparent, with increasing reinforcement particle size for both fatigue and monotonic fracture surfaces. No evidence of SiC particles protruding from the fatigue fracture surfaces was apparent for the encapsulation-processed composites (Fig. 7a–c). The R-curve fracture surfaces of the encapsulation-processed composites (Fig. 7d–f), and both fatigue and R-curve surfaces of the mixed/cast composite (Fig. 8a, b), all displayed extensive evidence of exposed SiC particles. However, only the 1 μm particle size composite (EP1) showed evidence of failure during R-curve testing by primary void growth

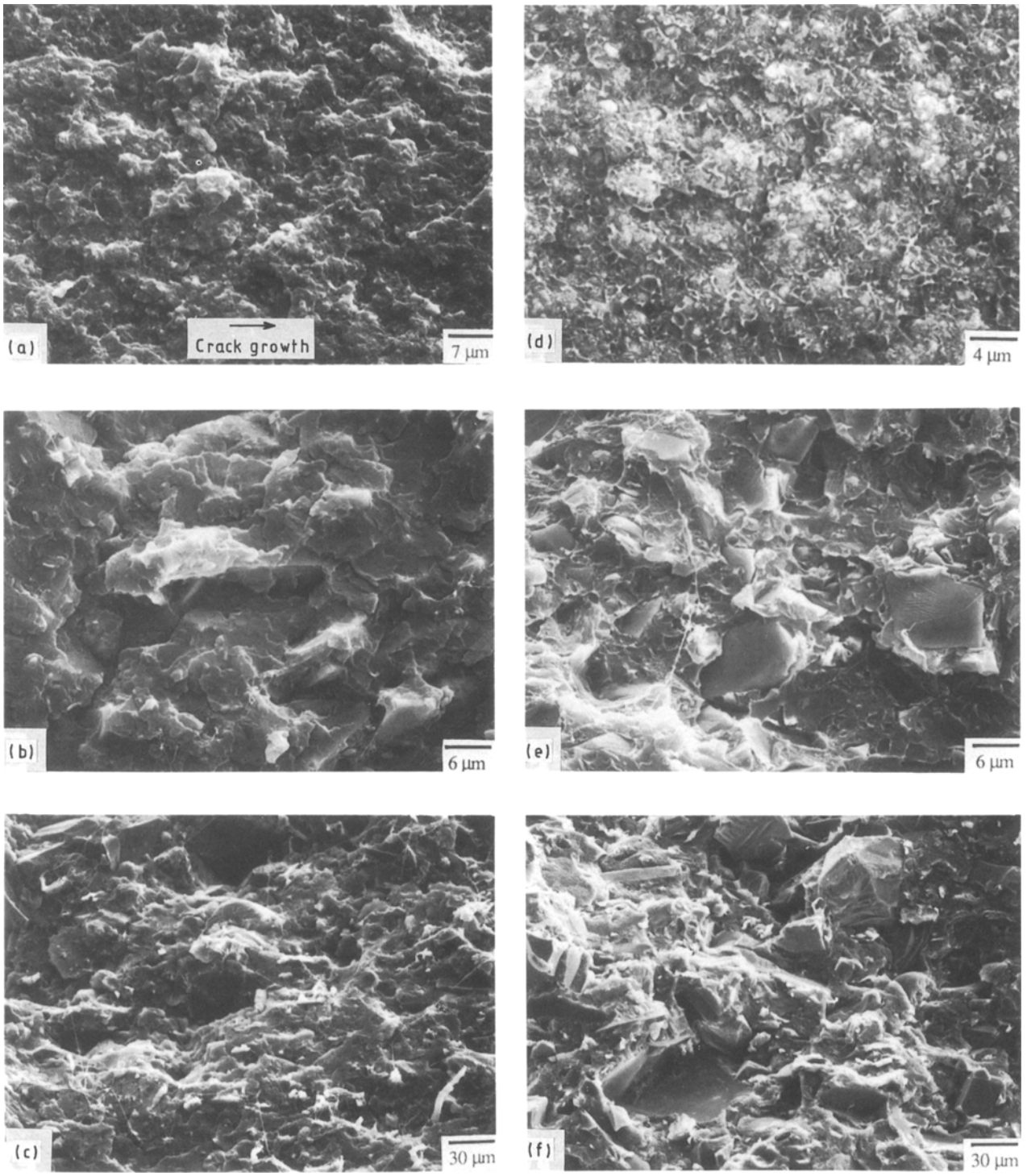

Figure 7 Representative SEM micrographs of the fracture surfaces of encapsulation-processed (EP) composites obtained under (a–c) fatigue and (d–f) R-curve loading conditions. Adjacent micrographs are of composites reinforced with the same particle size, namely (a, d) 1 μm, (b, e) 16 μm and (c, f) 100 μm. Arrow in (a) indicates general direction of crack growth for all micrographs.

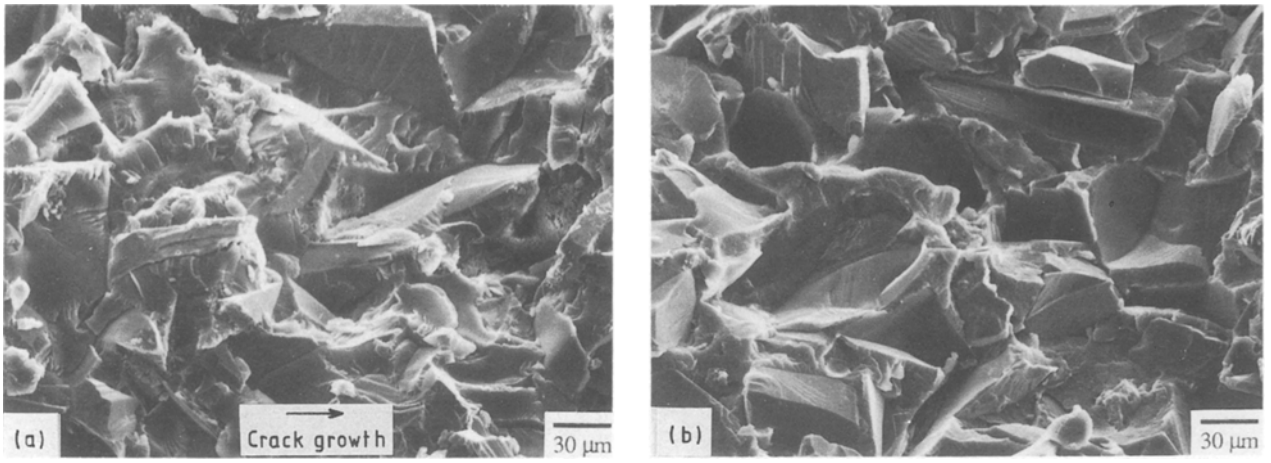

Figure 8 Representative SEM micrographs of the fracture surfaces of the cast/mixed (CC) composite reinforced with 100 μm SiC particles obtained under (a) fatigue and (b) R-curve loading conditions. Arrow in (a) indicates general direction of crack growth for both micrographs.

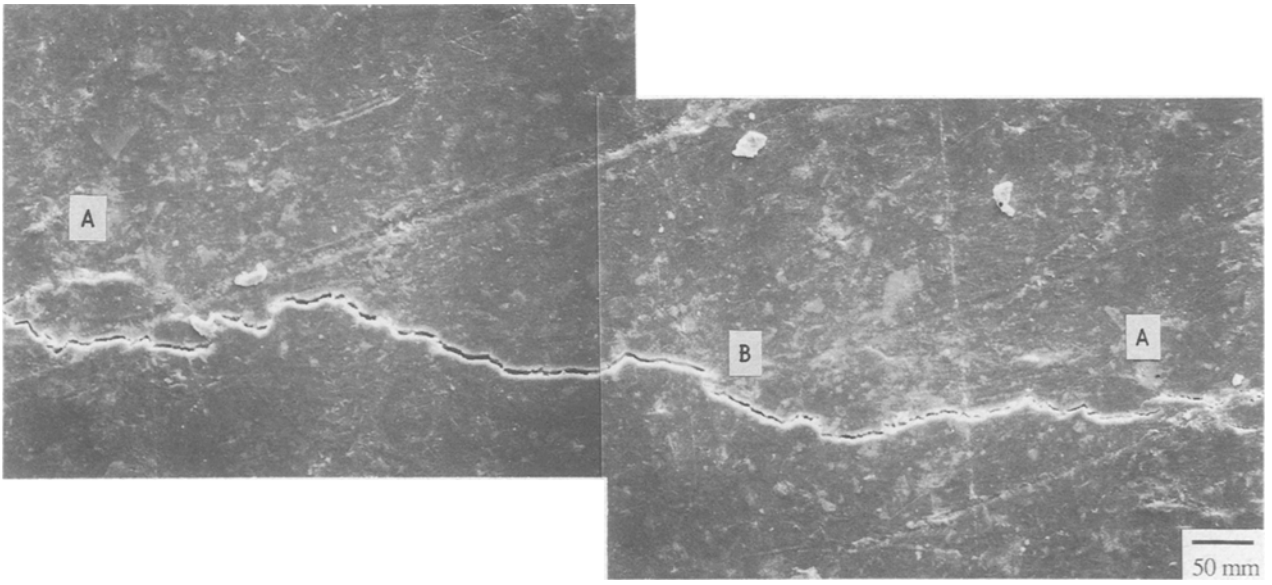

Figure 9 SEM micrograph showing a typical crack profile of the encapsulation-processed PMMA-matrix composite exhibiting crack bridging by overlapping ligaments (designated by A) and co-planar ligaments (B).

and coalescence, producing a ductile cup–cone fracture morphology. Reinforcement particles were observed in the fracture surface voids, indicating that they may have been initiated by the particles (Fig. 7d). This behaviour was not observed for the larger particle sizes.

Closer examination of the fatigue fracture surfaces revealed some evidence of step-like fatigue striations across the polymer matrix (Fig. 7b), consistent with reported observations of fatigue behaviour in neat resin PMMAs [16]. Also in evidence on all fracture surfaces are exposed microfibrils which indicate craze development during fracture. Crazes are interpenetrating networks of voids and highly stretched polymer that develop in high-stress regions such as those found ahead of a crack tip. Craze development during crack propagation has previously been reported for many glassy polymers, including PMMA [16, 20].

A typical crack path is shown in profile in Fig. 9. Evidence of crack bridging by uncracked matrix regions spanning the crack surfaces are clearly apparent. Both overlapping of the main crack and co-planar ligaments from fracture occurring ahead of the crack tip were observed. Such evidence of crack bridging suggests that crack-tip shielding plays a significant role in composite toughening.

4. Discussion

4.1. Processing

The encapsulation process was optimized by varying the concentrations of reactants and nucleation sites within solution until a stable heterogeneous nucleation regime was reached. When reactant concentration is too high, uncontrolled homogeneous nucleation occurs in the bulk of solution. This is illustrated by a LaMer diagram, where the monomer concentration profile is plotted versus time and the homogeneous and heterogeneous nucleation regimes are shown (Fig. 10a). A reduction in homogeneous nucleation

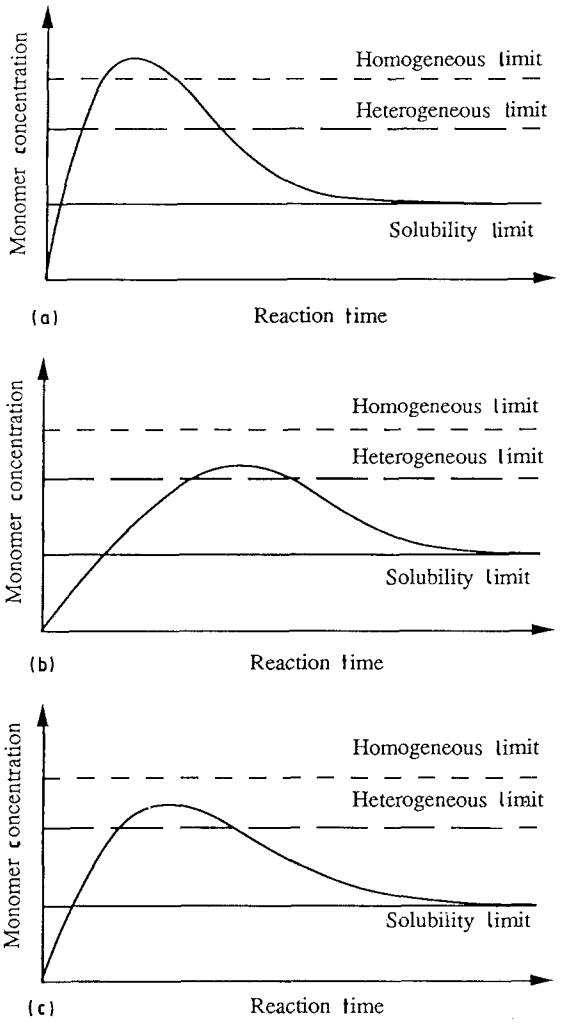

Figure 10 LaMer diagram indicating the effects of process variables on polymer nucleation showing (a) the monomer concentration profile as a function of time, (b) reduction of the slope of the profile from monomer dilution, and (c) increasing the nucleation sites resulting in suppression of homogeneous nucleation.

can be achieved by either decreasing the concentration of reactants by means of further monomer dilution, or by increasing the number of nucleation sites available. Further monomer dilution reduces the slope of the concentration profile (Fig. 10b). Conversely, increasing the concentration of nucleation sites increases the consumption of monomer in the heterogeneous nucleation regime, thereby delaying or altogether suppressing homogeneous nucleation (Fig. 10c).

In extremely dilute monomer solutions, the reaction concentration can be precisely varied, thereby controlling the rate of polymer deposition and giving greater control over the coating thickness. Polymer loadings of 1.5–2% have been achieved [10], where the polymer loading, PL, is defined as

$$PL = \frac{\mathrm{PMMA_{weight}}}{\mathrm{PMMA_{weight}} + \mathrm{SiC_{weight}}} \quad (5)$$

By increasing the number of possible nucleation sites, however, much higher loading can be achieved. Because of the desire to achieve high polymer loading, close coating thickness control was not attempted. Complete heterogeneous nucleation was achieved by first increasing the fraction of SiC to near the limit of suspendable concentration, followed by slowly decreasing the monomer concentration until the onset of homogeneous nucleation was suppressed.

The observed agglomeration of coated particles is consistent with that reported by Coker [10], who determined that interparticle agglomeration begins to occur at polymer loadings above approximately 3–6%. However, the critical polymer loading limit for agglomeration, PL_C, is dependent upon the specific nature of the polymer employed. For soft polymers such as polyethyl acetate, PL_C will be lower, whereas for hard polymers such as polymethyl methacrylate, PL_C will be substantially higher.

4.2. Crack growth behaviour

Addition of the particulate reinforcement phase appears in general to have enhanced both the toughness and resistance to fatigue crack growth of the polymeric-matrix composites. Such improvement was most apparent with the largest particle size (100 μm). Note, however, that while the resistance to fatigue crack growth was increased with particle size, crack growth was observed to occur over an increasingly narrow range of applied ΔK. Indeed, values of the exponent m in the growth-rate relationship (Equation 4) are significantly higher than those commonly reported for metals (typically 2 to 4) or polymers (typically 3 to 10) and closer to exponents reported for more brittle materials such as intermetallics and ceramics (typically 15 to 40) [21]. High values of m have significant implications for fracture mechanics-based life-prediction procedures for components [21, 22].

Details of the specific effect of the particles on toughness and fatigue crack growth may be elucidated by considering their role in influencing the fracture mode and the extent of crack-tip shielding. These interactions depend strongly on such variables as matrix plasticity, particle size, matrix–particle interface strength and residual stress states. Using typical values for the yield strength σ_y and Young's modulus E_{PMMA} of PMMA [23], estimates of the plastic zone size* r_p and the craze length l_c are presented in Table II. Estimates of the crack-tip opening displacements δ_c at K_c are also included in the table.

4.2.1. Fracture toughness

It is immediately apparent from Table II that EP1 containing 1 μm particle size reinforcements is the only composite in which the particle size is significantly smaller than estimates of the scale of local crack-tip plasticity. Depending on particle–matrix interface strength characteristics, these particles may be expected to interact with the fracture mode producing nucleation sites for ductile microvoid formation. Indeed, SEM micrographs of the fracture surfaces of

* Linear elastic behaviour and small-scale yielding are assumed. More precise analysis of crack-tip plastic deformation should include the viscoelastic behaviour of PMMA.

TABLE II Estimates of plastic zone size, craze length and CTOD values at $K = K_c$ for the composites tested

Composite	Particle size (μm)	Maximum plastic zone size[a], r_p (μm)	Maximum craze length[b], l_c (μm)	Crack-tip opening displacement[c], δ_c (nm)
EP1	1	11	27	18
EP16	16	46	122	83
EP100	100	181	473	319
CC100	100	102	268	182

[a] Computed from $r_p = 0.15\,(K_c/\sigma_y)^2$ [24].
[b] Computed from $l_c = 0.4\,(K_c/\sigma_c)^2$ [20], where we assume the crazing stress $\sigma_c \simeq \sigma_y$.
[c] Computed from $\delta_c = 0.5\,(K_c^2/(E'\sigma_y)$ [25], where using a rule of mixtures, E' of the composite was obtained from typical values of E_{PMMA} and E_{SiC}.

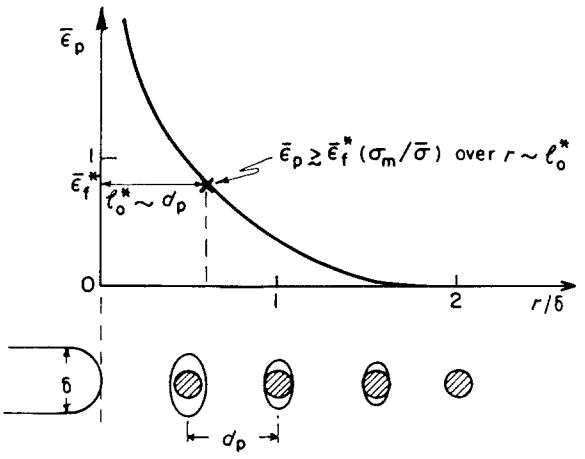

Figure 11 Schematic illustration of the stress-modified critical strain model for ductile fracture by microvoid growth and coalescence around particles [25].

EP1 indicate that the SiC reinforcement particles have, in fact, acted as ductile void initiation sites (Fig. 7d). Failure is reminiscent of ductile rupture in metals from microvoid coalescence [26] where fracture can be modelled using a stress-modified critical strain approach. The onset of ductile crack extension at $K = K_c$ is assumed when the local equivalent plastic strain $\bar{\varepsilon}_p$ exceeds a critical fracture strain $\bar{\varepsilon}_f^*$ over a characteristic microstructural dimension l_0^*, comparable with the void-initiating particles (Fig. 11). This approach, which has been used successfully in predicting fracture in ductile metals with pre-existing voids [26], yields [27]

$$K_c \propto (E'\sigma_0\bar{\varepsilon}_f^* l_0^*)^{0.5} \quad (6)$$

where E' is the effective Young's modulus for plain strain and σ_0 is the yield stress. Note that at the point of void impingement, the critical fracture strain $\bar{\varepsilon}_f^*$ is proportional to $\ln(d_p/D_p)$, where d_p and D_p are the mean void spacing and size, respectively [28]. From this analysis it is apparent that while $\bar{\varepsilon}_f^*$ may be expected to remain approximately constant (from simple geometrical considerations), l_0^* decreases with smaller particle size. For the present study, therefore, it may be concluded that where particle sizes are smaller than the extent of local plasticity, decreasing fracture toughness may be expected with smaller particle sizes.

Alternatively, when the reinforcement particles are comparable in size to the extent of crack-tip plasticity, crack–particle interactions may take other forms depending strongly on the particle–matrix interface strength. For the present composites, analysis of the cast composite fracture surfaces reveals clean SiC particle surfaces, indicating complete interfacial debonding with relatively brittle cleavage-like failure of the matrix. In contrast, the encapsulation-processed composites reveal reduced debonding of the SiC particles and a more fibrous failure of the matrix. Such differences in the extent of particle debonding and matrix failure mode may be related to residual stresses introduced during processing.

Shear mixing requires the introduction of particle reinforcement at an intermediate stage of polymerization, while viscosity is low. At this stage of polymerization, matrix contraction is only partially complete. The polymerization of methyl methacrylate produces a net volume decrease (ΔV) of 28%, as determined by the ratio of densities ($\rho_{MMA} = 0.936\,g\,cm^{-3}$, $\rho_{PMMA} = 1.2\,g\,m^{-3}$). During casting, the matrix is constrained from shrinking by both the mould walls and the dispersed particles. These constraints produce triaxial tensile stresses within the matrix, which weaken the particle–matrix interface and result in poor mechanical properties of the matrix.

By contrast, the residual stress levels of encapsulation-processed composites are much lower. SEM micrographs confirm that the failure mode is a mixture of matrix crazing and interfacial debonding. Since the matrix has been fully polymerized before consolidation, only thermal mismatch stresses are introduced into the composite. As a result, the particle–matrix interface stays intact to a higher applied stress level with increased matrix ductility (fracture strain). In this case, second-phase particles may be expected to impede crack advance in a manner similar to hardening from dislocation–particle interactions. This phenomenon of crack trapping [29] has been reported for crack growth in particulate-reinforced metal-matrix composites [30].

Controlled particle–matrix debonding may result in additional toughening mechanisms, namely zone shielding (microcrack toughening) [31], crack deflection [32] and crack bridging [33]. Toughening from zone shielding results from interfacial debonding/microcracking in a zone of material surrounding the

crack. The resulting dilated zone is similar to that obtained during transformation toughening and may provide significant shielding of the crack tip [31]. However, excessive debonding degrades the material ahead of the crack tip to such an extent that the overall resistance to crack propagation is reduced. Similarly, excessive debonding reduces the effectiveness of crack deflection. Rather than being forced around the obstacles, the crack is attracted to the debonded interfaces.

Finally, significant toughening may be derived from crack bridging. Where the reinforcement phase is sufficiently strong and the reinforcement/matrix relatively weak, growth of a crack through the matrix may leave the intact reinforcement phase spanning the crack at locations behind the crack tip. Energy dissipation in the resulting bridging zone from frictional sliding at the interface provides the potent toughening seen, for example, in fibre-reinforced brittle-matrix composites [34]. Alternatively, energy dissipation from plastic stretching of ductile-phase reinforcements may provide similar beneficial toughening effects as seen, for example, in rubber-toughened polymers [35]. However, in the present SiC-particle reinforced polymers, similar to particulate-reinforced metal-matrix composites [33] and continuously reinforced ductile-matrix composites [36], analysis of crack profiles reveals a different mechanism for bridging: that of uncracked matrix ligaments spanning the crack surfaces (Fig. 9).

While a complete analysis of the mechanics of matrix ligament bridging is beyond the scope of the present study, several simple models have been constructed to account for its potent shielding potential [33]. Increased bridging zone length, area fraction of uncracked ligaments, strain to failure and strength of the matrix ligaments, all contribute to an increased shielding capacity of the bridging zone. The greater ductility of the encapsulation-processed EP100 matrix may therefore have a significant effect on enhancing shielding from bridging compared to the less ductile CC100 matrix which contains pre-existing residual tensile stresses and strains from shear/mix processing.

4.2.2. Fatigue crack growth

Unlike fracture under monotonic loading, analysis of the fatigue fracture surfaces revealed that the crack had completely avoided the reinforcement particles for the encapsulation-processed composites (Fig. 7a–c). No debonding of the particle–matrix interface was observed, presumably due to the lower stress fields encountered during fatigue crack growth. Conversely, the weaker particle–matrix interface of the shear-mixed composite showed extensive debonding with SiC particles clearly visible on the fatigue fracture surface (Fig. 8a).

The enhanced resistance to fatigue crack growth observed for composites with progressively coarser reinforcement particle sizes is primarily attributed to the increasingly rough fracture surfaces. When viewed in profile, the increasingly tortuous path necessitated for the crack to avoid the coarser particles is immediately apparent. The benefits of such a meandering crack path for improved resistance to fatigue crack growth are: (i) growth rates are effectively reduced by the longer path length of the crack, (ii) the local stress intensity at the crack tip is reduced whenever the crack deviates from the plane of maximum tensile stress (crack deflection mechanisms), and (iii) the local near-tip stress intensity range is reduced due to enhanced roughness-induced crack closure.

Using a simple two-dimensional model for a crack with prediodic tilts through an angle ϕ, where the lengths of the linear and deflected segments are c and s, respectively, the reduced local crack-tip stress intensity range, ΔK_{tip}, can be related to the nominal applied ΔK by [32]

$$\Delta K_{tip} \approx \left(\frac{c \cos^2(\phi/2) + s}{c + s} \right) \Delta K \qquad (7)$$

The apparent average crack growth rate of the tilted crack (da/dN) due to the longer crack path is similarly given by

$$\frac{da}{dN} \approx \left(\frac{c \cos \phi + s}{c + s} \right) \left(\frac{da}{dN} \right)_L \qquad (8)$$

where $(da/dN)_L$ is the growth rate of the linear (undeflected) crack. It is therefore apparent that increasingly rough deflected crack paths (increasing ϕ and c/s ratios) result in both a reduced crack driving force and a lower apparent crack growth rate. However, assuming a maximum deflection of $\phi = 75°$ with $c/s = 1$ results in predicted reductions of $\approx 20\%$ which, although significant, does not appear to account for the 67 to 95% improvements in ΔK_{TH} observed for the coarser particulate composites.

Alternatively, the presence of SiC particles which are significantly larger than estimates of the maximum crack-tip opening displacements (CTOD) in Table II presents a potentially potent source of crack closure. Such premature closing of the crack from asperity contact of the rough fracture surfaces behind the crack tip results in a significantly reduced crack-tip stress intensity range $\Delta K_{tip} = K_{max} - K_{cl}$, where the closure stress intensity $K_{cl} \geqslant K_{min}$. Particularly at low load ratios, roughness-induced closure has been shown to result in high closure loads approaching 80% of K_{max} in particulate-reinforced metal-matrix composites [30]. Although not measured in the present study, similar elevated closure loads are indicative of the increasingly rough fracture surfaces for the coarser particulate reinforcement, providing a significant source of crack-tip shielding.

Finally, it is interesting to note that while the toughness of the encapsulation-processed composite EP100 exhibited a marked improvement compared to the cast/mixed CC100 composite, no similar improvement of fatigue crack growth resistance was apparent. Such behaviour is typical in many material systems where fracture modes under monotonic and cyclic loading conditions may be sensitive to the effects of different microstructural features. In the current study, resistance to fatigue crack growth is dominated primarily by the roughness characteristics of the fatigue fracture

path and relatively insensitive to particle–matrix debonding and matrix ductility. In marked contrast, fracture toughness is highly sensitive to debonding characteristics and the strain to failure of the matrix material.

5. Conclusions

The results of this study clearly indicate that the choice of processing route has a significant effect on fracture toughness and little effect on the fatigue-crack propagation resistance of particulate-reinforced polymeric-matrix composites. The following conclusions are drawn:

1. The R-curve behaviour of the encapsulation-processed composite versus the more traditional cast/mixed composite reveals a 33% improvement in fracture toughness. Higher residual stress and strain levels within the cast composite, together with excessive particle–matrix debonding, diminish the toughening contribution from crack bridging by uncracked matrix ligaments.

2. By contrast, no significant improvement was noted for fatigue-crack growth resistance; these results are rationalized in terms of the sensitivity of fatigue-crack growth to fracture surface morphology and a relative insensitivity to matrix ductility.

3. Increasing fracture toughness and resistance to fatigue-crack growth was observed with increasing reinforcement particle size. Such trends are consistent with increasing contributions from mechanisms of crack-tip shielding.

Acknowledgements

This work was supported by the Director, Office of Energy Research, Office of Basic Energy Sciences, Materials Sciences Division of the US Department of Energy under Contract No. DE-AC03-76SF00098 at the Lawrence Berkeley Laboratory.

References

1. S. MALL, G. M. NEWAZ and M. FARHADINIA, *J. Reinf. Plast. Compos.* **6** (1987) 138.
2. L. J. BROUTMAN and S. SAHU, *Mater. Sci. Eng.* **8** (1971) 98.
3. K. L. TRACHTE and A. T. DIBENEDETTO, *Int. J. Polym. Mater.* **1** (1971) 75.
4. P. K. MALLICK and L. J. BROUTMAN, *Mater. Sci. Eng.* **18** (1975) 63.
5. F. F. LANGE and K. C. RADFORD, *J. Mater. Sci.* **6** (1971) 1197.
6. A. J. KINLOCH, D. L. MAXWELL and R. J. YOUNG, *ibid.* **20** (1985) 4169.
7. Y. A. DZENIS, *Mech. Compos. Mater.* **22** (1986) 12.
8. L. E. NIELSEN, *J. Compos. Mater.* **1** (1967) 100.
9. L. E. HORNBERGER and K. L. DeVRIES, *Polym. Eng. Sci.* **27** (1987) 1473.
10. J. N. COKER, US Patent 3 897 586 (1975).
11. ASTM Standard E. 647-86a, in "1987 ASTM Annual Book of Standards", Vol. 3.01 (American Society for Testing and Materials, Philadelphia, 1987) p. 899.
12. K. KENDALL, *J. Mater. Sci.* **22** (1987) 4514.
13. R. H. DAUSKARDT and R. O. RITCHIE, *Closed Loop* **17** (1989) 7.
14. P. K. LIAW, H. R. HARTMANN and W. A. LOGSDON, *J. Testing Eval.* **11** (1983) 202.
15. ASTM Standard E. 399-83, in "1987 ASTM Annual Book of Standards", Vol. 3.01 (American Society for Testing and Materials, Philadelphia, 1987) p. 680.
16. R. W. HERTZBERG, in "Deformation and Fracture Mechanics of Engineering Materials" (Wiley, New York, 1989) p. 598.
17. P. C. PARIS and F. ERGDOGAN, *ASME J. Basic Eng.* **85** (1963) 528.
18. R. H. DAUSKARDT, D. B. MARSHALL and R. O. RITCHIE, *J. Amer. Ceram. Soc.* **73** (1990) 893.
19. F. ZOK and C. L. HOM, *Acta Metall. Mater.* **38** (1990) 1895.
20. R. W. LANG, J. A. MANSON, R. W. HERTZBERG and R. SHIRRER, *Polym. Eng. Sci.* **24** (1984) 833.
21. R. H. DAUSKARDT, M. R. JAMES, J. R. PORTER and R. O. RITCHIE, *J. Amer. Ceram. Soc.* **75** (1992) 759.
22. R. O. RITCHIE and R. H. DAUSKARDT, *J. Ceram. Soc. Jpn* **99** (1991) 1047.
23. M. F. ASHBY, *Acta Metall.* **37** (1989) 1273.
24. D. M. TRACEY, *J. Engng Mater. Tech.* **98** (1976) 146.
25. C. F. SHIH, *J. Mech. Phys. Solids* **29** (1981) 305.
26. R. H. DAUSKARDT, R. D. PENDSE and R. O. RITCHIE, *Acta Metall. Mater.* **35** (1987) 2227.
27. R. O. RITCHIE, W. L. SERVER and R. A. WULLAERT, *Metall. Trans.* **10A** (1979) 1557.
28. J. R. RICE and D. M. TRACEY, *J. Mech. Phys. Solids* **17** (1969) 201.
29. J. R. RICE, in Proceedings of 20th ASTM Symposium, edited by R. P. Wei and R. P. Gangloff (American Society for Testing and Materials, Philadelphia, 1989) in press.
30. J. K. SHANG and R. O. RITCHIE, *Acta Metall.* **37** (1989) 2267.
31. A. G. EVANS, S. WILLIAMS and P. W. R. BEAUMONT, in "Ceramic Containing Systems – Mechanical Aspects of Interfaces and Surfaces" ed. A. G. Evans (Noyes, Park Ridge, New Jersey, 1986) p. 286.
32. S. SURESH, *Metall. Trans.* **14A** (1983) 2375.
33. J. K. SHANG and R. O. RITCHIE, *Met. Trans.* **20A** (1989) 897.
34. A. G. EVANS and D. B. MARSHALL, *Acta Metall.* **37** (1989) 2567.
35. A. G. EVANS, Z. B. AHMAD, D. G. GILBERT and P. W. R. BEAUMONT, *ibid.* **34** (1986) 79.
36. B. N. COX and D. B. MARSHALL, *Fat. Fract. Eng. Mat. Struct.* **14** (1991) 847.

Received 20 December 1991
and accepted 11 August 1992